In-operando study of chemical expansion and oxygen surface exchange rate in epitaxial $GdBaCo_2O_{5.5}$ electrodes in a solid-state electrochemical cell by time-resolved X-ray diffraction

Arindom Chatterjee, Jose Manuel Caicedo, Belén Ballesteros and Jose Santiso *

Catalan Institute of Nanoscience and Nanotechnology (ICN2); CSIC and Barcelona Institute of Science and Technology (BIST), Bellaterra-08193, Spain

Abstract:

This report explores the fundamental characteristics of epitaxial thin films of mixed ionic electronic conducting $GdBaCo_2O_{5.5\pm\delta}$ (GBCO) material with layered perovskite structure, relevant for use as an active electrode for the oxygen reduction and evolution reactions in electrochemical devices. Time-resolved X-ray diffraction in combination with voltage step chrono-amperometric measurements in a solid state electrochemical cell provide a deeper insight into the chemical expansion mechanism in GBCO electrode. The chemical expansion coefficient along *c*-axis, α_c, shows a negative value upon the compound oxidation contrary to standard perovskite materials with disordered oxygen vacancies. Chemical expansion also shows a remarkable asymmetry from α_c= -0.037 to -0.014 at δ<0 and δ>0, respectively . This change in chemical expansion is an indication of a different mechanism of the structure changes associated with the variable Co cation oxidation state from $Co^{2+}\rightarrow Co^{3+}\rightarrow Co^{4+}$. Since the redox reactions are dominated by the oxygen surface exchange between the GBCO electrode and gas atmosphere, monitoring the time response of the structure changes allows for direct determination of oxygen reduction and evolution reaction kinetics. The reaction kinetics are progressively slowed down upon reduction in the δ<0 oxygen stoichiometry region, while they maintain a high catalytic activity in the δ>0 region, in agreement with the structural changes and the electronic carrier delocalization when crossing δ=0. This work validates the time-resolved XRD technique for fast and reversible measurements of electrode activity in a wide range

of oxygen non-stoichiometry in a solid-state electrochemical cell operating under realistic working conditions.

1. **Introduction**

In electrochemical devices like solid oxide fuel cells (SOFCs) and oxygen permeation membranes the kinetics of the Oxygen Reduction Reaction (ORR), related to the oxygen surface exchange between the gas atmosphere and the electrode materials, often limits the overall performance of the device.[1,2] Large activation energies of these reactions at the SOFC cathodes cause large polarization losses when reducing operating temperatures below 800 °C.[3] Therefore, gaining a deeper knowledge of ORR mechanisms and rates of cathode materials has been a major challenge in the development of competitive intermediate-temperature SOFC technology.[4,5] To this end, a variety of cathode materials have been proposed from composite materials[6-8] to mixed ionic-electronic materials.[9-13]

Studies of oxygen surface exchange in cathode materials are generally performed by electrochemical impedance spectroscopy,[14] conductivity relaxation[15,16] or isotopic exchange depth profiling combined with SIMS or LEIS analysis.[17-21] Recently, time-resolved X-ray diffraction,[22-27] wafer curvature relaxation monitoring[28] as well as optical absorption experiments,[29] have emerged as powerful methods to determine surface exchange kinetics in thin film electrodes through monitoring subtle crystal structure and optical transient changes in the material induced by oxide stoichiometry changes when exposed to sudden changes in the pO_2 gas atmosphere. Other external stimuli, such as the application of an electric field between the electrode material and a solid electrolyte, typically Yttria-stabilized zirconia (YSZ) material, can also cause a perturbation from the equilibrium changing the oxygen stoichiometry. The study of the transient structure changes by in-situ XRD after electrical stimuli have also proven to be an effective method to explore redox reaction mechanisms in $SrCoO_x$ films[30] and to determine kinetics of oxygen surface exchange reactions in classical perovskite electrode materials such as $La_{1-x}Sr_xCo_{1-y}Fe_yO_{3-\delta}$.[22-24]

The present study focuses on the determination of the mechanisms of chemical strain and oxygen surface exchange rate in a less conventional double perovskite material: $GdBaCo_2O_{5.5\pm\delta}$ (GBCO). GBCO compound, as the rest of the members of the *A*-site ordered $LnBaCo_2O_{5+\delta}$ family (*Ln*: La, Pr, Nd, Sm, Gd, Y), have attracted much attention because of their mixed ionic and electronic conductivity and high temperature stability as well as catalytic activity for oxygen reduction and evolution reactions, which make them interesting candidates as cathode materials in intermediate temperature solid oxide fuel cells (IT-SOFC). [19, 31-34] GBCO material suffers from large thermal expansion compared to compatible electrolytes, which makes it difficult to use in SOFC stacks.[32] In oxygen permeation membranes $LnBaCo_2O_{5+\delta}$ ceramics have exhibited reduced oxygen permeation.[35] However, the fact that these compounds could show a reduced chemical expansion compared to classical perovskites, still makes them ~~ideal~~ attractive for oxygen permeation membranes, where large chemical potential gradients often cause mechanical failure by crack formation or delamination during operation. [36,37]

$GdBaCo_2O_{5.5\pm\delta}$ compound has a layered perovskite structure with GdO and BaO layers alternating in the *A*-sites of the perovskite structure along *c*-axis direction. This produces a doubling of the cell parameter.[38] Stoichiometric compound $GdBaCo_2O_{5.5}$ with δ=0 holds a large oxygen non-stoichiometry compared with a fully occupied perovskite structure with 50% of oxygen vacancies at the oxygen sites of $GdO_{0.5}$ planes maintaining full occupancy of oxygen sites in BaO and CoO_2 planes. These oxygen vacancies order along *b*-axis forming alternating fully occupied and vacant rows parallel to *a*-axis, thus also doubling *b*-axis parameter. This forms the so called 1x2x2 orthorhombic structure. Related to this particular layered structure, GBCO, as the rest of $LnBaCo_2O_{5+\delta}$ compounds, shows anisotropic chemical expansion enlarging the *c*-axis parameter and contracting along *a, b*-axis upon oxidation,[39,40] behaving similarly to $La_2NiO_{4+\delta}$ layered compound with K_2NiF_4 structure, which incorporates oxygen interstitials as dominant oxide defects in the $0<\delta<0.15$ range. [41,42] In a polycrystalline material the *c*-axis expansion is compensated by the *a,b*-axes compression and therefore the overall cell volume expansion is considerably reduced. The use of epitaxial thin films allows exploring the chemical strain

behaviour in a defined crystallographic direction. At the same time in epitaxial films the surface exchange reactions are related to characteristic crystal planes at the thin film surface, which allow for a closer correlation of catalytic activity with theoretical models.[43,44] This study makes use of the time-resolved XRD technique in an electrochemical cell with different applied voltage to address both chemical strain and oxygen surface exchange rates in a wide range of oxygen non-stoichiometry, without changing the PO_2 atmosphere.

2. Experimental section

A 200 nm $GdBaCo_2O_{5.5}$ (GBCO) thin film was grown on a yttria-stabilised zirconia (YSZ) single crystal substrate (5 x 5 x 0.5 mm^3) with (001) orientation (from Crystec, GmbH) by using pulsed laser deposition (PLD). Deposition conditions for epitaxial *c*-axis oriented GBCO where previously optimised (substrate temperature T_s= 850 °C, laser energy fluence of 1.5 J/cm^2, laser repetition rate=10Hz, and oxygen partial pressure PO_2= 60 mTorr).[19] A thin layer of $Ce_{0.8}Gd_{0.2}O_2$ material (CGO) was PLD deposited between GBCO and YSZ to avoid the typical chemical reaction, forming $BaZrO_3$ at the same conditions as for GBCO.[45] The complete GBCO/CGO/YSZ heterostructure was analysed by X-ray diffraction (XRD) to assess the quality of the epitaxial growth. High resolution transmission electron microscopy (HRTEM) was used to observe cross section images of the deposited hereostructure in a FEI Tecnai G^2 F20 microscope with a field emission gun working at 200kV.

For the electrochemical characterisation a Pt top electrode (50 nm thick) was deposited on the GBCO film surface over 0.4 mm∗ 0.5 mm area by using the PLD technique through a hard mask. Special care was taken to avoid deposition of Pt on the sides of the GBCO/CGO/YSZ cell in order to prevent current leakage during the electrical measurements. For the electrochemical cell characterisation Ag paste was used to paint a porous electrode covering all the bottom side of the YSZ crystal. Top and bottom electrodes were contacted with thin Ag wires. In order to perform in-situ combined X-ray diffraction and electrochemical characterisation the thin film heterostructure was placed in a

PANalytical X'Pert Pro MRD lab diffractometer equipped with a DHS 900 domed heating chamber from Anton Paar. The chamber allows for the control of the gas atmosphere and was adapted to feed through the electrical connections. The full experimental set up is depicted in Fig. 1.

The sample was heated up to 350 °C in 1 atm of synthetic air flow (21% O_2 and 79% N_2 pure gases mixture) in order to have sufficient oxide ion conductivity in the YSZ electrolyte (at 350 °C expected YSZ conductivity is about 10^{-5} S/cm)[46]. This also guarantees the achievement of sufficient oxygen exchange at the interface between the top GBCO and bottom Ag electrodes and the gas atmosphere, which is also necessary for the electrochemical stabilisation of a current flow.

Positive and negative voltage bias steps from 0, ±100, ±200 and ±300 mV were applied to the electrodes and the electrical current transients were monitored continuously. Special care was taken to avoid sample heating by Joule effect at large voltages, which could add a thermal expansion contribution to the chemical expansion. This is the reason why the voltage was limited only to ±300mV. Voltage was first changed from 0V to +100mV and maintained for 20-30 min until a stationary regime was established. The applied voltage was then reset back to 0V for 20-30 min. A subsequent cycle at -100mV was set with the same time span. This procedure was followed for increasing voltages of ±200 mV and ±300mV.

Simultaneously, the structure cell parameters of the GBCO material (*c*-axis parameter) were continuously monitored by XRD by following the angular shift of one particular diffraction peak (004) in fast 2θ static scans every 10 sec making use of a multichannel X-ray detector (PIXcel from Panalytical). For the best accuracy of the cell parameter determination we used a 2 x Ge(220) monochromator to use only CuKα_1 radiation. A complete description of the time-resolved X-ray diffraction procedure has been previously described in.[25-27]

3. Results and Discussion

Fig. 2 corresponds to a TEM cross section of the GBCO/CGO/YSZ thin film heterostructure in low magnification (Fig. 2a), as well as a high resolution detail around the CGO buffer layer, showing the high quality of the GBCO/CGO and CGO/YSZ interfaces and the perfect *c*-axis oriented growth of the GBCO layer (Fig. 2b). FFT images in Fig. 2c are obtained from selected areas of the GBCO and CGO layers. They show their relative orientations with [001]GBCO//[001]CGO//[001]YSZ along the film growth direction (vertical) and [110]GBCO//[100]CGO//[100]YSZ along the in-plane direction (horizontal). In respect of the contrast in the GBCO image along the film growth direction, every two perovskite blocks correspond to the GdO-BaO alternate arrangement of the double perovskite structure parallel to *c*-axis.

Fig. 3a shows the room temperature X-ray diffraction pattern of the GBCO/CGO/YSZ (001) heterostructure. The observation of intense 00L reflections from GBCO indicates the full *c*-axis orientation of the epitaxial film. Reflections 004 and 008 corresponding to the CGO buffer layer were also observed close to the intense 00L peaks from YSZ single crystal substrate. There is no indication of any chemical reaction at the interface forming $BaZrO_3$ (typically appearing as a peak at $2\theta=43°$). For comparison the figure also shows the XRD pattern of a GBCO/YSZ heterostructure deposited under the same conditions but without the CGO interlayer, which showed the formation of the $BaZrO_3$. This proves the effectiveness of the CGO layer to prevent the reaction, as well as preserving the epitaxial growth of GBCO. The XRD reciprocal space map in Fig 3b corresponds to an area containing -204 YSZ, -204 CGO and -116 GBCO asymmetric reflections. The different values of Q_x in-plane component for CGO and GBCO compared to YSZ indicate that there is no substantial epitaxial strain in the heterostructure. Room temperature cell parameters of GBCO were estimated from these measurements as follows: out-of-plane c = 7.546 Å and in-plane a= $b/2$= 3.928 Å (estimated from -116 GBCO reflection along [110] direction is an average of a, $b/2$ cell parameters) very close to reported bulk values a= $b/2$= 3.897 Å and c= 7.572 Å.[40]

A. Current intensity changes

Fig. 4 shows the current measurements after the different voltage steps measured at T= 350 °C in 1 atm air atmosphere (pO_2= 0.21 atm). In the first voltage step a change from 0 V to +100 mV the current produced an instantaneous increase to about 18.1 μA. It then displayed a transient behaviour following an exponentially decay in about 20 min to a current of 15.6 μA. This stabilization should correspond to the time it takes to equilibrate the oxygen exchange rates at the film electrode/air surface and at the film electrode/electrolyte interface before reaching a steady state, as described in ref [22]. When resetting the voltage to 0V the current dropped to a negative value -3.1 μA and exponentially went to zero recovering the initial state. When a negative voltage step from 0V to -100 mV was applied the current initially decreased to -17.0 μA and exponentially stabilized at -12.7 μA. The increase in the voltage produced a proportional increase in the initial current peak and subsequent current intensity decay. At V= ±300 mV the current showed fluctuations of a large magnitude that precluded extraction of any reliable current value. However, the corresponding transient current values when switching off the voltage to 0V showed perfect exponential decays in the full voltage range from 100 to 300 mV. Their respective time responses were analysed by fitting simple exponential decay curves.

B. Cell parameter changes

The corresponding cell parameter changes at 350 °C were monitored during the same voltage steps as shown in Fig. 5a. When applying a positive bias from 0V to +100mV (anodic potential) GBCO c-axis parameter increased from c= 7.5992 Å following an exponential curve until an almost constant value c=7.6008 Å was reached at +100mV. The increase in c-parameter in GBCO is explained by an increase in oxygen stoichiometry. This indicates that anodic potential causes an oxidation reaction injecting oxygen into the GBCO film. Despite the very small change in cell parameter of about $\Delta c/c$= +0.021% the high accuracy in the XRD measurement of the relative cell parameter changes of about 10^{-4} Å allowed for chemical strain determination and curve fitting to extract a meaningful value of the oxygen exchange time response. When the potential was switched off from +100 mV to 0 V, the c-parameter decreased exponentially to the initial

equilibrium value. This means that oxygen is released from the GBCO film lattice (reduction process) in a reversible way. When applying a negative bias voltage step from 0V to -100mV (cathodic potential) the reverse situation occurred and the GBCO *c*-axis parameter shrank to 7.5975 Å, corresponding to a $\Delta c/c$= -0.028%. Fig. 5b depicts the measured $\Delta c/c$ relative change for the different bias voltage. As can be observed the *c*-parameter proportionally increases with anodic potential and it tends to saturate at +300 V where *c*-parameter changes reach $\Delta c/c$ = +0.044% expansion. However, for the negative bias there is a much steeper reduction of the cell parameter reaching $\Delta c/c$ = -0.102% at V= -300 mV, which is more than twice the cell parameter change at a positive bias of the same magnitude. This is an indication of a clear asymmetry in the GBCO cell expansion.

The asymmetry in the chemical strain could be related to two possible causes: i) either the change in oxygen stoichiometry $\Delta\delta$ could be different for a given magnitude of the bias voltage depending on its sign, or ii) in the case of a similar oxygen stoichiometry change, the corresponding chemical expansion (or more generally the chemical strain, i.e. the relative change in cell volume per $\Delta\delta$) may not be exactly symmetric, corresponding to a different mechanism for oxidation and reduction.

C. Oxygen non-stoichiometry determination

In order to differentiate between these two possibilities the chronoamperometry was used to analyse the oxygen stoichiometry changes, $\Delta\delta$. The transient decay in the measured current when a voltage was set (or reset) is related to the injected charge into GBCO (electrons from the top Pt electrode or oxide ions from the YSZ electrolyte) as in a normal capacitor. However, the material stays electrically neutral because of redox reactions establishing charge compensation. A steady state is achieved when electrical current from the electrodes is balanced with the oxygen flow produced by the oxygen surface exchange between GBCO and air atmosphere. If one assumes, as a rough approximation, that the whole GBCO film achieves a homogeneous oxygen stoichiometry, the change in δ can be estimated simply by calculating the area under the current versus time curve between the initial and steady state values:

$$Q = \int_{t=0}^{t=\infty} I(t)dt \qquad (1)$$

Therefore, the transported charge *Q* for the whole film volume will be directly related to the stoichiometry change $\Delta\delta$ per unit cell volume:

$$\Delta\delta = \frac{Q}{n.e}\left(\frac{V_{unit\ cell}}{V_{thin\ film}}\right) \qquad (2)$$

where *n*=2 is the number of electrons per oxygen O^{2-} ion, and *e* is the electron charge.

Note that it is still not possible to estimate the absolute value of the oxygen stoichiometry - only the relative change from the equilibrium state at 350 °C in air (PO_2= 0.21 atm).

As an example of the calculation, Fig. 6a shows a detail of the exponential current decay after applying a positive voltage bias step from 0V to +100mV. A transported charge of 864 μC was calculated after integration of the dashed area under the curve. As there are 2 electrons involved in the redox reaction for each O^{2-} ion and the number of unit cells in the thin film are known parameters (number of unit cells = total film volume 5 x 5mm^2 x 200 nm thickness / unit cell volume) the oxygen stoichiometry change corresponds in this case to $\Delta\delta$ = +0.06 (assuming the double perovskite cell $GdBaCo_2O_{5.5\pm\delta}$). For a comparison of these values with those of other compounds, like fluorites or perovskites with different oxide concentration per unit volume, the oxygen stoichiometry change $\Delta\delta$ should be normalized to the molar fraction of oxide ions in the stoichiometric compound, as described in ref [47]. Therefore, in this case it should be divided by 5.5, so the normalized $\Delta\delta^N$ for the abovementioned case becomes $\Delta\delta^N$ = +0.011. Since it is likely that there is an oxygen stoichiometry inhomogeneity in GBCO depending on the lateral distance from the top Pt electrical contact due to the GBCO sheet resistance causing an effective voltage decay along the film the calculated $\Delta\delta^N$ can only be taken as an approximation for the qualitative

comparison between the different voltages, provided the oxygen composition inhomogeneity is comparable for the various experimental conditions.

Fig. 6b shows the calculated $\Delta\delta$ values for the cathodic and anodic voltages for the on (0 to V) and off (V to 0) voltage step change. The values obtained for the on and off steps for a particular bias voltage are almost the same, which corresponds as expected to the reversibility of the oxidation and reduction process, and it proves the validity of the calculation. At the highest voltage values ±300 mV, either positive or negative, the $\Delta\delta$ content seems to have reached a saturation level, particularly at negative bias voltage, where no increase in $\Delta\delta$ is observed between -200 and -300 mV voltage steps. This is in contrast with the *c*-axis parameter values which still show a change in such higher voltages. The most remarkable result is that the $\Delta\delta$ values attained for positive and negative bias voltages are very symmetric indicating that there is no substantial difference in the energy cost for the oxygen vacancies formation. A larger energy needed to fill (or to generate) an oxygen vacancy for positive bias voltage would make the oxygen non-stoichiometry change $\Delta\delta$ to be lower than for a negative bias voltage of the same magnitude. In consequence, this observation rules out the hypothesis that the larger relative *c*-parameter change at negative bias depicted in Fig. 5b may be related to a larger non-stoichiometry compared to positive bias, and unambiguously points towards an asymmetric chemical expansion. With the applied voltages of V= $\pm$300mV at 350 °C the attained $\Delta\delta$ reaches about $\pm$0.135. This oxygen non-stoichiometry relative change corresponds to an equivalent span in pO_2 of about 6 orders of magnitude obtained for GBCO in a previous coulometric titration experiment at 900 °C.[44] This proves the potential of the electrochemical method in comparison to gas phase stabilization for generating a non-stoichiometry in mixed valence oxide compounds at reduced temperatures.

D. Chemical expansion coefficient

Taking advantage of the calculated oxygen stoichiometry changes Fig. 6c depicts the relative *c*-axis variations, the strain ε_c observed along the *c*-axis, as a function of the change in $\Delta\delta^N$. The slope represents the chemical expansion coefficient as defined in [47]. The most remarkable result is that in the whole

stoichiometry range analysed from $GBCO_{5.34}$ to $GBCO_{5.64}$ the cell expands upon incorporation of oxygen as opposed to classical perovskites and fluorites where the increase in oxygen stoichiometry, and therefore the reduction of the oxygen vacancy concentration, causes the shrinkage of the cell. Since the chemical expansion coefficient α_c is generally defined to be positive as the cell expands upon an increase in the concentration of oxide vacancies following

$$\varepsilon = \alpha_c [V_O^{\cdot\cdot}] \quad (3)$$

for the particular case of GBCO α_c shows a negative value along *c*-axis. Negative values of α_c have generally been observed in perovskite-related layered compounds with K_2NiF_4 structure, such as in $La_2NiO_{4+\delta}$ [49] or $Nd_{2-x}Sr_xNiO_{4+\delta}$ [50] along *c*-axis where the dominating oxygen defects correspond to oxide intertitials $[O_i^{''}]$ which incorporate into rock salt layers sandwiched between perovskite block layers. The *c*-axis expansion is related to the coulomb repulsion between perovskite blocks when varying the relative charge of the rock salt layers. The reported value of the chemical expansion coefficient along *c*-axis in $La_2NiO_{4+\delta}$ is α_c (∥*c*)= -0.076 (being $\Delta\delta^N$ normalized to the oxide molar concentration). Since in these materials the chemical expansion is rather anisotropic α_c (∥*a*)= +0.028, the overall chemical expansion is compensated α_{vol} (average)= +0.002.[49] These materials are therefore of special interest for electrochemical applications where the material is exposed to large differences in the oxygen chemical potential and large expansions can cause failure of the device, for example, in oxygen separation membranes or electrodes in solid oxide fuel cells and solid electrolysers.

In the case of GBCO, the particular behaviour of the *c*-axis expansion upon increasing the oxygen composition in GBCO can be regarded as a competition between the $[GdO_\delta]$ block expansion and [BaCoO] compression (at least in the range $GBCO_{5.5\pm\delta} < 5.5$).[51] The incorporation of oxygen fills the oxygen vacancy sites in the $[GdO_\delta]$ slabs and causes their expansion due to Coulomb repulsion. The oxygen sites in the [BaCoO] slabs are fully occupied, and therefore, no oxygen stoichiometry variations are expected in this slab. However, the charge generated by the incorporation of oxygen in the $[GdO_\delta]$ slabs should be

compensated by transferring two electrons per O ion coming from the mixed valence Co ions. Therefore, the oxidation state of Co increases, which implies a reduction of its ionic radius. This produces a compression of the [BaCoO] that opposes the [GdO_δ] slab expansion. The same reasoning can be used for the reduction of the oxygen stoichiometry. The overall *c*-axis variation is a balance between the change in both the slabs and it seems to be dominated by the [GdO_δ] expansion making the GBCO behave differently from typical oxygen vacancy disordered perovskites and more similarly to some layered oxides with K_2NiF_4 structure.

Returning to the experimental results depicted in Fig. 6c, it is clear that the chemical expansion coefficient shows a nonlinear dependence in the oxygen stoichiometry range explored by the electrochemical reduction and oxidation. Qualitatively, it shows an average slope of $\alpha_c = 0.014$ at $\Delta\delta>0$, and a larger value $\alpha_c = 0.037$ at $\Delta\delta<0$. In the absence of clear phase transitions, the differences in the chemical expansion coefficient are expected to arise from changes in the oxygen vacancy concentrations, along with concomitant changes in the oxidation state of the transition metal cations, affecting its effective ionic radius. In this region, the chemical expansion is often referred to as stoichiometric expansion, as extensively described by Bishop *et al*.[52] It cannot be ruled out that at larger values of $\Delta\delta$ non-stoichiometry there are phase changes resulting from either a spin state transition, oxygen vacancies order-disorder transition, or charge order in Co^{2+}/Co^{3+} or Co^{3+}/Co^{4+}. This fact would need a more accurate study of the cell structure variation.

The asymmetry in the cell expansion magnitude observed for positive and negative voltage bias could be then related to some differences in the [GdO_δ] and [BaCoO] chemical expansion counterbalance. As a first approximation a qualitative explanation can be inferred in terms of changes in the Co oxidation state. According to Shannon the Co ionic radii for the octahedral (VI-) coordination are[53]

Oxidation state	Co^{2+}	Co^{3+}	Co^{4+}

Ionic radius* (crystal radius) (in Å)	0.79 [LS] 0.885 [HS]	0.685 [LS] 0.75 [HS]	0.67 [HS]

where HS and LS are high and low spin states, respectively. Although the coordination and spin state of the Co ions in the GBCO structure are far more complex that the compounds from which the ionic radii were extracted, this approach can still serve as a qualitative guide to estimate the changes in the ionic radii. In the GBCO films it can be assumed that the equilibrium oxygen stoichiometry is close to $GdBaCo_2O_{5.5}$ ($\delta \sim 0$), which corresponds to a pure Co^{3+} oxidation state, in either LS or HS state. Then, a positive bias will favour the $Co^{3+} \rightarrow Co^{4+}$ oxidation, while a negative bias will cause $Co^{3+} \rightarrow Co^{2+}$. In the case that the change in Co ionic radius was the dominant effect in the overall cell expansion variations, and assuming the [GdO_δ] expansion to behave uniformly in the whole $\Delta\delta$, any substantial change in the $Co^{2+} \rightarrow Co^{3+}$ or $Co^{3+} \rightarrow Co^{4+}$ steps will produce a certain asymmetry between positive and negative bias. If we consider only the high spin values, the difference in the ionic radii between Co^{2+}(HS)$\rightarrow Co^{3+}$(HS) is -18%, while for Co^{3+}(HS)$\rightarrow Co^{4+}$(HS) it is -11%. In this case, the oxidation causes a larger shrinkage of the [BaCoO] block, a factor of 1.6 times larger in the negative bias than for positive bias. Since this change is opposite to the [GdO_δ] block expansion, the overall contribution to the cell expansion would result in a smaller chemical strain coefficient for negative bias compared to positive bias, in contrast to the experimental observation. Therefore, a different combination of spin states should be considered. If one assumes Co^{2+}(LS)$\rightarrow Co^{3+}$(HS)$\rightarrow Co^{4+}$(HS), the relative changes in ionic radii are -5.3% and -10.7%, respectively. In this case, the oxidation will produce a larger contraction opposed to the [GdO_δ] block expansion, which still remains dominant, but will therefore result in a smaller (still positive) chemical expansion coefficient, in agreement with the present observation. Although this relative change in the [BaCoO] compression of about a factor 2.0 approaches that

observed in the experimental *c*-axis expansion, $((\Delta c)_{-0.2V}/(\Delta c)_{+0.2V} = 2.3)$ is still of a lower magnitude. Further analyses have to be performed to evaluate the spin state of the Co ions, in order to ascertain the correspondence with the chemical expansion coefficients. Additionally, an accurate structural characterisation in the $5.5+\delta$ region will indicate whether the expansion mechanisms of the two separate $[GdO_\delta]$ and [BaCoO] blocks still behave as in the reported $5.5-\delta$ oxygen stoichiometry range.[51] It cannot be ruled out that the $[GdO_\delta]$ slabs induce an additional asymmetry because of the incorporation of oxygen into the empty oxygen column sites (parallel to *a*-direction) causing an oxygen vacancy site disorder that may affect the Gd-O coordination and have some impact onto the cell parameters. Another contribution to consider is the possible change in charge localization. Most of the explanations argued to establish a simple correspondence between chemical expansion and ionic radii derive from a large degree of charge localization. In the presence of delocalization, the effective ionic radius is no longer related to that included in Shannon's database and can induce a lower chemical expansion. This could be the case for GBCO in the $5.5+\delta$ composition region where $Co^{3+} \rightarrow Co^{4+}$ induces more itinerant electronic carriers and larger electronic conductivity in comparison to the $5.5-\delta$ composition region with $Co^{3+} \rightarrow Co^{2+}$.

E. Asymmetry in time response

The analysis of the time response of current transients with different applied voltages also manifests a clear asymmetry between positive and negative bias. Fig. 7 depicts the different values of the time constants τ obtained from the transitory decay response fit to single exponential curves both for the current transients and for the simultaneous *c*-axis parameter changes for the OFF step voltage change (from $\pm$V to 0V). In the current measurements for positive voltages, we measured similar time responses of $\tau \sim 220$ sec from +100mV, 200mV and +300mV, regardless of the on or off voltage step. However, for negative bias voltages, the time response increases linearly from $\tau \sim 220$ sec, to 295 sec and 350 sec, at -100V, -200mV and -300mV, respectively. The time responses obtained for the *c*-axis parameter change for the same voltage steps show slightly lower values, although they follow the same trend. Since the

overall time response should be determined by the slowest process in a series of steps (rate determining step) one can assume that it is dominated by the variations in the oxygen surface exchange rate at the surface of the GBCO film, which is believed to be the slowest of the electrochemical processes involved. The characteristic length for oxygen diffusion in the GBCO film across *c*-axis is expected to be much larger than the film thickness and therefore the effect of oxide ionic diffusion on the transient current and cell expansion is negligible in the films. We also assume that oxygen exchange reactions at the bottom Ag/YSZ electrode and interfacial oxide ionic exchange between the GBCO film and the GDC/YSZ electrolyte are not rate limiting. Under these assumptions the Oxygen Reduction Reactions (ORR) at positive bias, and Oxygen Evolution Reactions (OER) under negative bias, at the GBCO surface determine the observed exchange rates. The ORR and incorporation into the lattice can be described by the following reactions:

$$\tfrac{1}{2}\, O_2(g) + V_O^{\bullet\bullet} + 2e^- \rightarrow O_O^x$$

and $$2Co(III)^x \rightarrow 2Co(IV)^{\bullet} + 2e^-$$

or $$2Co(III)^x + 2e^- \rightarrow 2Co(II)'$$

depending on whether the Co^{3+} ions oxidize to Co^{4+} or reduce to Co^{2+}.
The exchange rate involves the availability of both oxygen vacancy sites and electronic charges. In this case, the remarkable change in the slope between the time response after the application of positive and negative bias should be induced by an important change in the defect chemistry. The equilibrium non-stoichiometry at the conditions of the experiment in air (PO_2= 0.21 atm, 350 °C, and 0 V) is expected to be close to $GdBaCo_2O_{5.5\pm\delta}$ ($\delta \sim 0$). This corresponds to a dominant Co^{3+} oxidation state. However, it is generally assumed that in Co perovskite oxides the high electric conductivity observed at elevated temperature is dominated by the Co disproportionation reaction:

$$2Co(III)^x \rightarrow Co(II)' + Co(IV)^{\bullet}$$

thus, producing mobile *e* and *h* carriers.[54] Since $\Delta\delta=0$ stoichiometry separates two regions with clearly different electric properties, at higher oxygen content (positive δ) the presence of Co^{3+}/Co^{4+} provides the material with dominant *p*-type electronic mobile charge carriers. However, at negative $\Delta\delta$ the presence of Co^{2+}/Co^{3+} turns it into *n*-type conductivity. The asymmetry observed in this work points towards a larger mobility of *p*-type carriers compared to *n*-type, possibly due to electron localization, therefore reducing the electrical conductivity at $\Delta\delta<0$. The slight difference in current and *c*-axis time response may arise from a slight difference in the surface reaction steps for ORR and OER at the position of the free exposed film (where the XRD measurements are centred, an average of the illuminated area of 1mm x 3mm) in comparison with the reactions taking place in the area below the Pt top electrode (which present a larger contribution to the current transient measurement). Smaller differences would be expected if XRD and current measurements where probing the exact same regions. This was not possible in the present experiment because of the large absorption of the X-rays through the deposited Pt electrode. A different geometry of the top Pt electrode, either thinner or porous, or mesh electrodes would be necessary to allow the same positioning for in-situ XRD and current measurements

Conclusions

In summary, in this work we have electrochemically oxidised and reduced epitaxial thin films of a complex mixed valence transition metal oxide, in a controlled and reversible way, making use of a solid-state electrochemical cell. This allowed in-situ analysis by XRD of very subtle associated structural changes, which led to an accurate study of the chemical strain mechanisms in $GdBaCo_2O_{5.5\pm\delta}$ epitaxial films, which showed a remarkable asymmetry in the chemical strain around $\delta=0$. At the same time, coupled time-resolved XRD and potential step chronoamperometry experiments allowed obtaining the time response of the oxidation and reduction processes, associated with the oxygen surface exchange rates. The asymmetry of the chemical strain observed between oxidation and reduction was also reflected in the surface exchange rates, being faster for oxidation compared with reduction, where the exchange rates become progressively slower. Provided that thin films can be prepared on

a YSZ solid electrolyte single crystal substrate, this method can be generalized for studying different complex solid state redox processes in a wide range of oxygen non-stoichiometry.

Acknowledgements

The authors acknowledge the support from projects: MINECO ref. MAT2016-77100-C2-1-P; CNRS-CSIC PICS Project ref. 261091, the EU for funding through project H2020-MSCA-RISE-2014 ref. 645658, and the AGAUR agency for 2017SGR. ICN2 is funded by the CERCA programme / Generalitat de Catalunya and by the Severo Ochoa programme of the Spanish Ministry of Economy, Industry and Competitiveness (MINECO, grant no. SEV-2013-0295). A.Ch. particularly acknowledges the support of Severo Ochoa programme for his PhD grant.

References

1 B. C. H. Steele, *Solid State Ionics*, 2000, **134**, 3–20.

2 S. B. Adler, *Chem. Rev.*, 2004, **104**, 4791–4844.

3 E. D. Wachsman and K. T. Lee, *Science*, 2011 **334**, 935-939.

4 J. Fleig, *Ann. Rev. Mater. Res.*, 2003, **33**, 361–382.

5 M. M. Kuklja, E. A. Kotomin, R. Merkle, Y. A. Mastrikov and J. Maier, *Phys. Chem. Chem. Phys.*, 2013 **15**, 5443–5471.

6 V. Dusastre and J. A. Kilner, *Solid State Ionics*, 1999, **126**, 163–174.

7 M. J. Jørgensen and M. Mogensen, *Journal of The Electrochemical Society*, 2001, **148**, A433–A442.

8 E. Perry Murray and S. A. Barnett, *Solid State Ionics*, 2001, **143**, 265–273.

9 B. C. H. Steele, *Solid State Ionics*, 1996, **86–88**, 1223–1234.

10 A. Tarancon, S. J. Skinner, R. J. Chater, F. Hernandez-Ramirez and J. A. Kilner, *J. Mater. Chem.*, 2007, **17**, 3175–3181.

11 J.-H. Kim, and A. Manthiram, *J. Mater. Chem. A*, 2015, **3**, 24195–24210.

12 A. Tarancon, M. Burriel, J. Santiso, S. J. Skinner, and J. A. Kilner, *J. Mater. Chem.*, 2010, **20**, 3799–3813.

13 J. A. Kilner, and M. Burriel, *Ann. Rev. Mater. Res.*, 2014, **44**, 365–393.

14 F. S. Baumann, J. Fleig, H. -U. Habermeier and J. Maier, *Solid State Ionics*, 2006, **177**, 1071–1081.

15 S. Wang, P. A. W. van der Heide, C. Chavez, A. J. Jacobson, and S. B. Adler, *Solid State Ionics*, 2003, **156**, 201–208.

16 B. Hu, Y. Wang, Z. Zhu, C. Xia and H. J. M. Bouwmeester, *J. Mater. Chem. A*, 2015, **3**, 10296-10302.

17 J. A. Kilner, S. J. Skinner, and H. H. Brongersma, The isotope exchange depth profiling (IEDP) technique using SIMS and LEIS. *J. Solid State Electrochem.*, 2011, **15**, 861–876.

18 H. Tellez, A. Aguadero, J. Druce, M. Burriel, S. Fearn, T. Ishihara, and J. A. Kilner, *J. Anal. At. Spectrom.*, 2014, **29**, 1361–1370.

19 J. Zapata, M. Burriel, P. García, J. A. Kilner and J. Santiso, *J. Mater. Chem. A* 2013, **1**, 7408-7414.

20 S. J. Skinner, and J. A. Kilner, *Solid State Ionics*, 2000, **135**, 709–712.

21 R. A. De Souza, J. A. Kilner, and J. F. Walker, *Materials Letters*, 2000, **43**, 43–52.

22 B. J. Ingram, J. A. Eastman, K. C. Chang, S. K. Kim, T. T. Fister, Perret, E. Perret, H. You, P. M. Baldo and P. H. Fuoss, *Appl. Phys. Lett.*, 2012, **101**, 051603.

23 E. M. Hopper, E. Perret, B. J. Ingram, H. You, K. -C. Chang, P. M. Baldo, P. H. Fuoss and J. A. Eastman, *J. Phys. Chem. C*, 2015, **119**, 19915–19921.

24 M. D. Biegalski, E. Crumlin, A. Belianinov, E. Mutoro, Y. Shao-Horn, and S. V. Kalinin, *Appl. Phys. Lett.*, 2014, **104**, 161910.

25 R. Moreno, P. García, J. Zapata, J. Roqueta, J. Chaigneau and J. Santiso, *Chem. Mater.* 2013, **25**, 3640-3647.

26 R. Moreno, J. Zapata, J. Roqueta, N. Bagués and J. Santiso, *J. Electrochem. Soc.*, 2014, **161**, F3046-F3051.

27 J. Santiso, R. Moreno (2017) In Situ High-Temperature X-ray Diffraction of Thin Films: Chemical Expansion and Kinetics. In: Bishop S., Perry N., Marrocchelli D., Sheldon B. (eds) Electro-Chemo-Mechanics of Solids. Electronic Materials: Science & Technology. Springer, Cham

28 J. D. Nicholas (2017) In Situ Wafer Curvature Relaxation Measurements to Determine Surface Exchange Coefficients and Thermo-chemically Induced Stresses. In: Bishop S., Perry N., Marrocchelli D., Sheldon B. (eds) Electro-

Chemo-Mechanics of Solids. Electronic Materials: Science & Technology. Springer, Cham

29 S. R. Bishop, J. J. Kim, N. Thompson, and H. L. Tuller, *ECS Transactions*, 2012, **45**, 491–495.

30 Q. Lu, and B. Yildiz, *Nano Letters*, 2016, **16**, 1186–1193.

31 A. Tarancón, A. Morata, G. Dezanneau, S. J. Skinner, J. A. Kilner, S. Estradé, F. Hernández-Ramirez, F. Peiro and J. R. Morante, *Journal of Power Sources*, 2007, **174**, 255–263.

32 N. Li, Z. Lü, B. Wei, X. Huang, K. Chen, Y. Zhang and W. Su, *Journal of Alloys and Compounds*, 2008, **454**, 274–279.

33 A. Tarancón, J. Peña-Martínez, D. Marrero-López, A. Morata, J. C. Ruiz-Morales and P. Núñez, *Solid State Ionics*, 2008, **179**, 2372–2378.

34 R. Pelosato, G. Cordaro, D. Stucchi, C. Cristiani, and G. Dotelli, *Journal of Power Sources*, 2015, **298**, 46–67.

35 K. Zhang, L. Ge, R. Ran, Z. Shao, and S. Liu, *Acta Materialia*, 2008, **56**, 4876–4889.

36 J. P. Kim, D. W. Pyo, E. Magnone, and J. H. Park, *Advanced Materials Research,* 2012, **560–561**, 959–964.

37 C. Bernuy-Lopez, K. Høydalsvik, M.–A. Einarsrud and T. Grande, *Materials*, 2016, **9**, 154.

38 A. Maignan, C. Martin, D. Pelloquin, N. Nguyen and B. Raveau, *J. Solid State Chem.*, 1999, **142**, 247–260.

39 P. S. Anderson, C. A. Kirk, J. Knudsen, I. M. Reaney and A. R. West, *Solid State Sciences*, 2005, **7**, 1149–1156.

40 A. A. Taskin, A. N. Lavrov, and Y. Ando, *Phys. Rev. B*, 2005, **71**, 134414.

41 V. V. Kharton, A. V. Kovalevsky, M. Avdeev, E. V. Tsipis, M. V. Patrakeev, A. A. Yaremchenko, E. N. Naumovich and J. R. Frade, *Chem. Mater.*, 2007, **19**, 2027–2033.

42 A. A. Yaremchenko, V. V. Kharton, M. V. Patrakeev, and J. R. Frade, *J. Mater. Chem.*, 2003, **13**, 1136–1144.

43 Y. Choi, D. S. Mebane, M. C. Lin, M. Liu, *Chem. Mater*., 2007, **19**, 1690–1699.

44 A. Kushima, S. Yip, and B. Yildiz, *Phys. Rev. B*, 2010, **82**, 115435.

45 A. Tarancón, J. Peña-Martínez, D. Marrero-López, A. Morata, J. C. Ruiz-Morales and P. Núñez, *Solid State Ionics*, 2008 **179**, 2372–2378.

46 C. Ahamer, A. K. Opitz, G. M. Rupp and J. Fleig, *Journal of The Electrochemical Society*, 2017, **164**, F790–F803.

47 D. Marrocchelli, C. Chatzichristodoulou and S. R. Bishop, *Phys. Chem. Chem. Phys.* 2014, **16**, 9229-9232.

48 D. S. Tsvetkov, V. V. Sereda and A. Yu. Zuev, *Solid State Ionics* 2010, **180**, 1620-1625.

49 V. V. Kharton, A. V. Kovalevsky, M. Avdeev, E. V. Tsipis, M. V. Patrakeev, A. A. Yaremchenko, E. U. Naumovich and J, R. Frade, *Chem. Mater.*, 2007, **19**, 2027–2033.

50 T. Nakamura, K. Yashiro, K. Sato and J. Mizusaki, *Solid State Ionics* ,2010, **181**, 402.

51 N. Ishizawa, T. Asaka, T. Kudo, K. Fukuda, A. Yasuhara, N. Abe and T. Arima, *Chem. Mater.*, 2014, **26**, 6503-6517.

52 S. R. Bishop, D. Marrocchelli, C. Chatzichristodoulou, N. H. Perry, M. B. Mogensen, H. L. Tuller and E. D. Wachsman, *Ann. Rev. Mater.*, Res. 2014, **44**, 205-239.

53 R. D. Shannon, *Acta Crystallographica*, 1976, **A32**, 751-767.

54 M. Yang, Y. Zhong, Z.-K. Liu, *Solid State Ionics*, 2007, **178**, 1027–1032.

Figure captions

Fig. 1. Experimental setup for the electrochemical cell characterization under controlled atmosphere inside the X-ray diffractometer temperature chamber.

Fig. 2. TEM cross section image of the GBCO/CGO/YSZ epitaxial heterostructure in low magnification (A). High resolution TEM image around the CGO buffer layer showing the perfect arrangement of the GBCO epitaxial layer with *c*-axis perpendicular to film plane (B). FFT images of selected regions of GBCO and CGO showing the relative orientation of film and substrate, with zone axes $[1\text{-}10]_{GBCO}$ and $[010]_{CGO}$, respectively. (C)

Fig. 3. (a) X-ray diffraction 2θ/ω pattern of the GBCO/CGO/YSZ(001) and GBCO/YSZ(001) heterostructures showing epitaxial growth with full *c*-axis orientation of GBCO; (b) Reciprocal space map around (-204)YSZ, (-204)CGO and (-116) GBCO reflections.

Fig. 4. Potential step chronoamperometry curves (*I* versus time transients) measured during the anodic and cathodic potential step voltage changes.

Fig. 5. (a) Variation of the GBCO *c*-axis parameter during the voltage changes as monitored by in-situ X-ray diffraction for the same voltages as in Fig.4. (b) Relative variation of the steady *c*-parameter when cathodic and anodic bias is applied. Strain in *c*-parameter is almost twice under anodic bias (positive voltage) than under cathodic potential (negative voltage). The lines are a mere guide to the eye.

Fig. 6. (a) Typical current intensity (*I*) transient used for the charge transfer measurement (corresponding to the anodic step voltage from 0 V to +100 mV); (b) corresponding oxide stoichiometry variations $\Delta\delta$ for the different cathodic and anodic voltage steps; (c) ε_c linear strain along *c*-axis for GBCO at the different oxide non-stoichiometry $\Delta\delta^N$ normalized to the oxygen molar fraction (the labels correspond to the chemical strain coefficients α_c as extracted from the slope of the curve).

Fig. 7. Characteristic time responses (τ) obtained from the transient curves of current (*I*) and *c*-axis variations measured on the GBCO film for anodic (V > 0) and cathodic voltage (V<0) steps. The graph includes τ values for the OFF step (from V to 0).

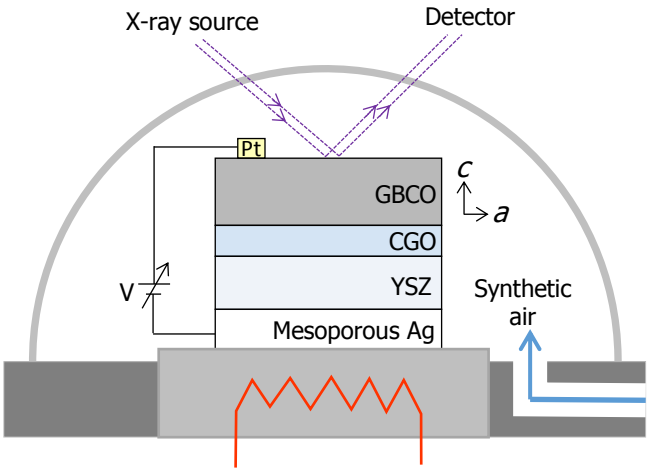
X-ray source
Detector
Pt
GBCO
CGO
YSZ
Mesoporous Ag
V
c
a
Synthetic
air

Figure 1

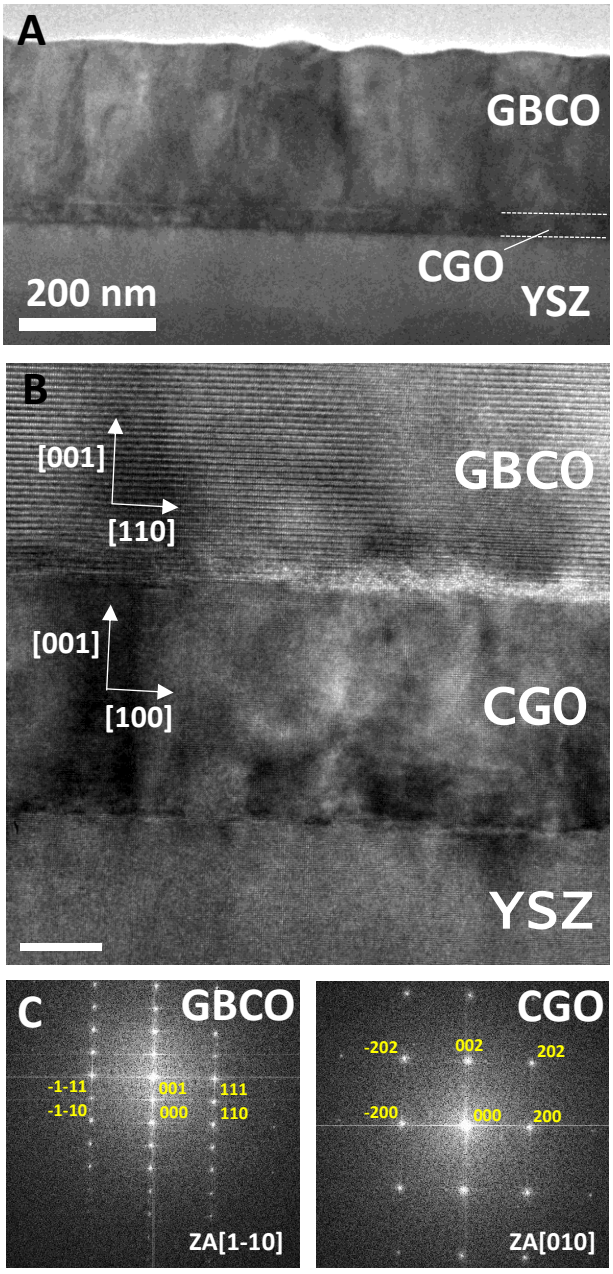
A
GBCO
CGO
YSZ
200 nm
B
[001]
[110]
GBCO
[001]
[100]
CGO
YSZ
C
GBCO
-1-11
-1-10
001
000
111
110
ZA[1-10]
CGO
-202
002
202
-200
000
200
ZA[010]

Figure 2

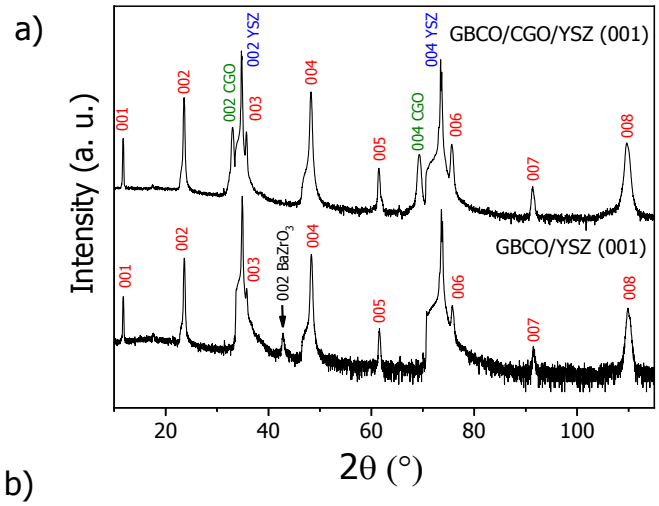
a)
GBCO/CGO/YSZ (001)
GBCO/YSZ (001)
001
002
002 CGO
002 YSZ
003
004
005
004 CGO
004 YSZ
006
007
008
002 BaZrO3
Intensity (a. u.)
20
40
60
80
100
2θ (°)

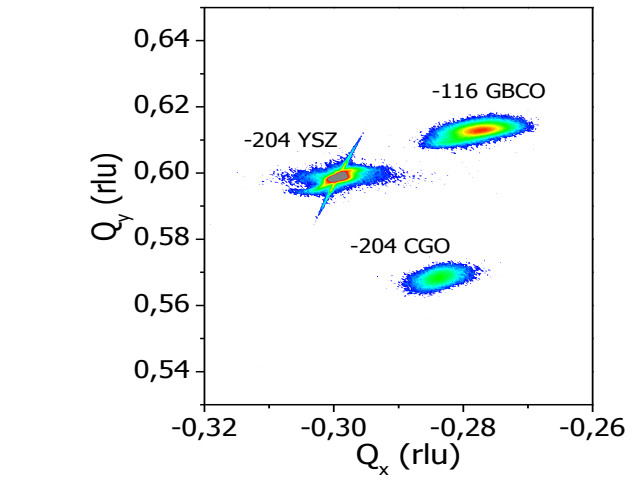
b)
-116 GBCO
-204 YSZ
-204 CGO
0,64
0,62
0,60
0,58
0,56
0,54
Qy (rlu)
-0,32
-0,30
-0,28
-0,26
Qx (rlu)

Figure 3

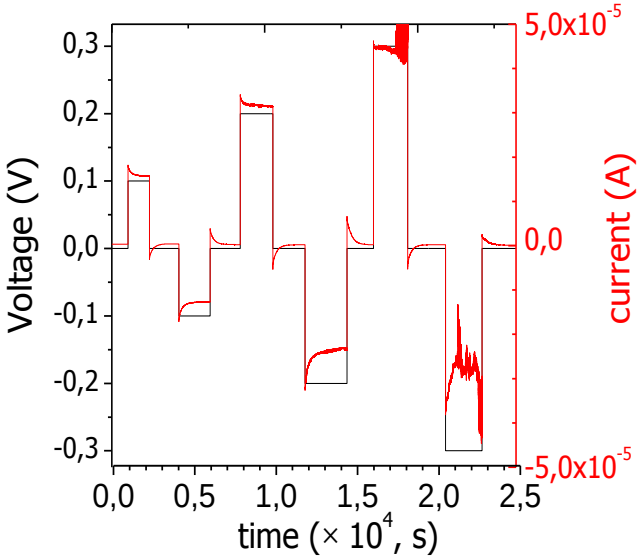
0,3
0,2
0,1
0,0
-0,1
-0,2
-0,3
Voltage (V)
0,0
0,5
1,0
1,5
2,0
2,5
time (× 10^4, s)
5,0x10^-5
0,0
-5,0x10^-5
current (A)

Figure 4

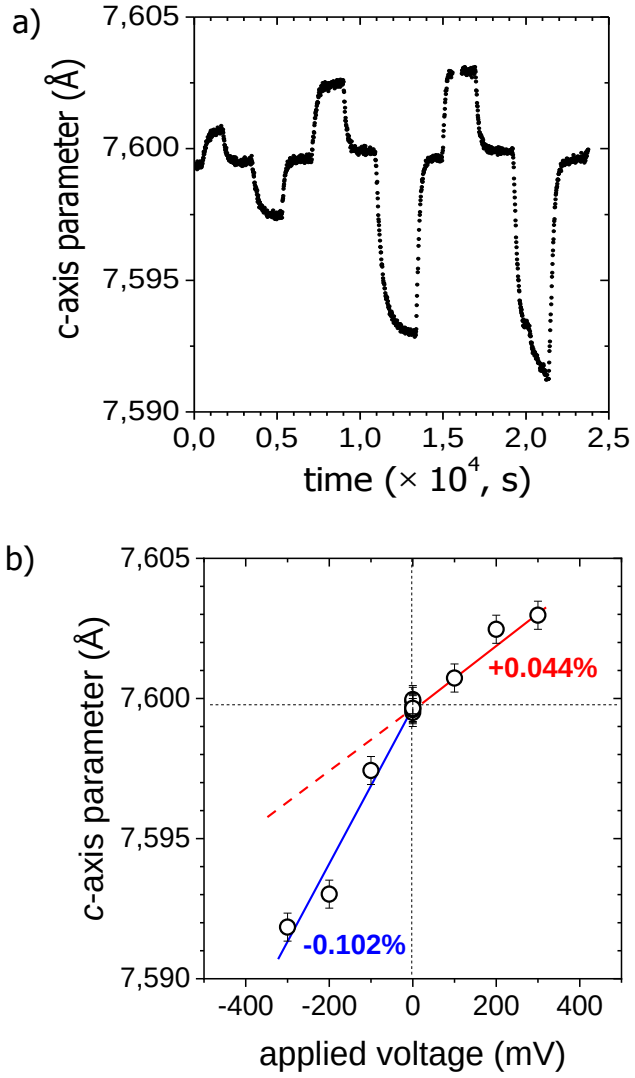
a)
7,605
7,600
7,595
7,590
c-axis parameter (Å)
0,0
0,5
1,0
1,5
2,0
2,5
time (× 10^4, s)
b)
7,605
7,600
7,595
7,590
c-axis parameter (Å)
+0.044%
-0.102%
-400
-200
0
200
400
applied voltage (mV)

Figure 5

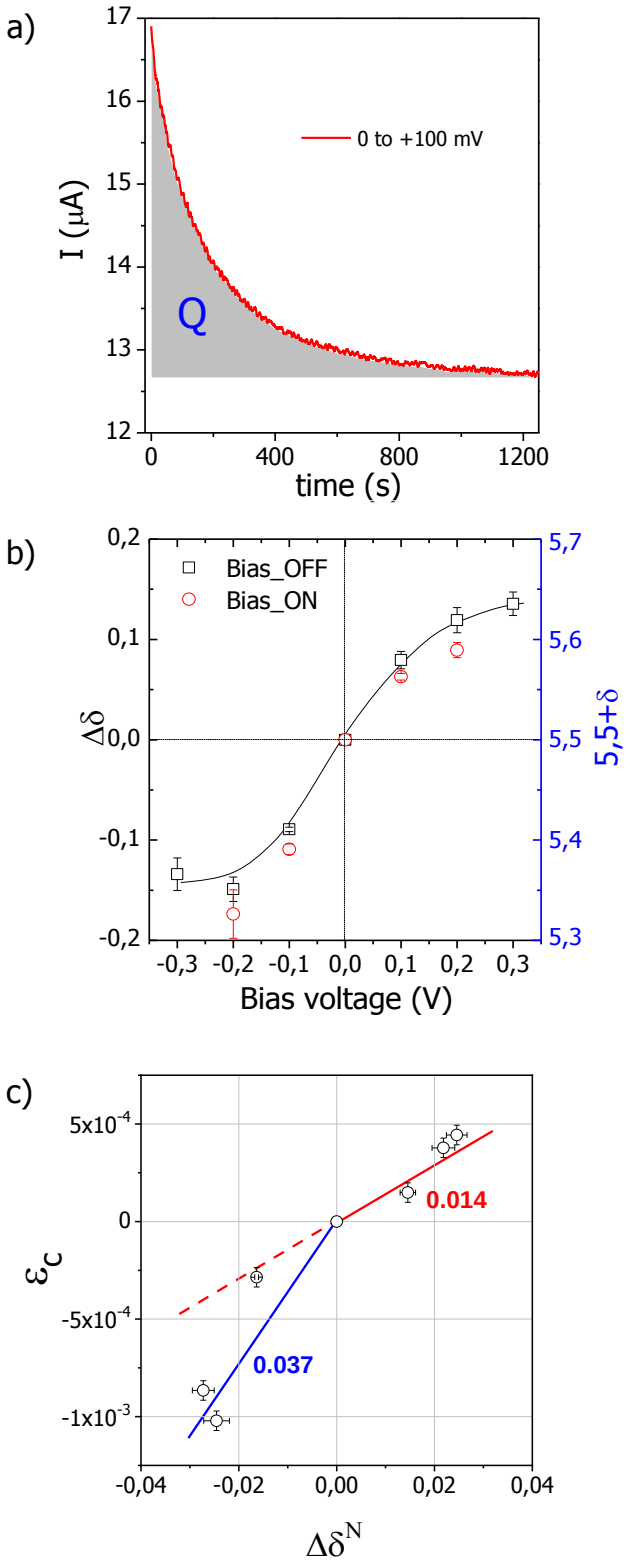
a)
I (μA)
time (s)
0 to +100 mV
Q
b)
Bias_OFF
Bias_ON
Δδ
5,5+δ
Bias voltage (V)
c)
ε_C
$\Delta\delta^N$
0.014
0.037

Figure 6

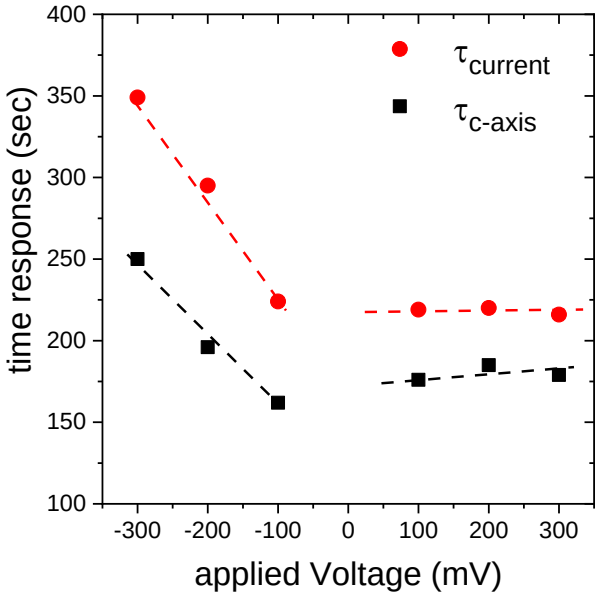
400
350
300
250
200
150
100
time response (sec)
-300
-200
-100
0
100
200
300
applied Voltage (mV)
τcurrent
τc-axis

Figure 7